Magnetism and piezoelectricity in stable transition metal silicate monolayers

Kayahan Saritas [1], Nassar Doudin,[2] Eric I. Altman [2], and Sohrab Ismail-Beigi [1,*]
[1]*Department of Applied Physics, Yale University, New Haven, Connecticut 06520, USA*
[2]*Department of Chemistry, Yale University, New Haven, Connecticut 06520, USA*

(Received 15 April 2021; revised 24 September 2021; accepted 8 October 2021; published 28 October 2021)

Two-dimensional van der Waals (2D vdW) single layered materials with ferromagnetism and piezoelectricity have been a subject of recent attention. Despite numerous reports of 2D ferromagnetic materials, developing an air stable and transferable vdW material has been challenging. To address this problem, we studied layered transition metal silicates that are derivatives of kaolinites and lizardites with transition metals substituting on Al^{3+} and Mg^{2+} sites using *ab initio* density functional theory calculations. This class of materials is appealing because they meet the symmetry requirements for piezoelectricity and can host a range of transition metal cations. As oxides, these materials are inherently stable in air. Following our previous experimental work, we predict that these compounds are stable under varying O_2 partial pressure and can be synthesized using a surface-assisted method. We also show that the oxidation states of the substituted transition metal ions can be tuned through the level of hydrogenation.

DOI: 10.1103/PhysRevMaterials.5.104002

I. INTRODUCTION

Two-dimensional van der Waals (2D vdW) materials that display ferromagnetism, piezoelectricity, and ferroelectricity have received increased attention [1–4]. vdW stacking of multiple 2D layers with these complementary properties can help develop multifunctional materials [5–7]. Despite the fact that there are various well-studied piezoelectric 2D materials available [8,9], developing an air-stable and transferable vdW single layered material whose ferromagnetism can be tuned under electric or elastic field has been challenging. Air stability is an important problem in this regard as it presents significant challenges in isolating and studying the single layers [10–13]. Single layers of CrI_3 [10], $Cr_2Ge_2Te_6$ [14], and $FePS_3$ [15] are also shown to be ferromagnetic, but similarly they suffer from sensitivity to oxidation. In comparison, the search space for ferroic oxide vdW layers remains underexplored. Oxides have the advantage of being stable under ambient conditions, e.g., most metals spontaneously form a thin layer of metal oxide on their surfaces [16].

Transition metal silicate sheets, which have been grown on metal substrates via annealing at elevated temperatures [17–19], are air-stable. Thanks to the open-shell transition metal atoms, their magnetic properties can also be tailored. Growing a 2D transition metal silicate starts with depositing Si or SiO and the transition metal ion, such as Ti [19], Fe [17], and Ni [18], at modest temperatures, which is then followed by annealing above 950 K. In all these cases, the transition metal silicate thermodynamically competes with the formation of bilayer SiO_2 [20–24]. However, parameters such as annealing time, temperature, oxygen pressure, Si, and transition metal coverage can facilitate metastable phase formation. As 2D Ti silicate [19] can be grown on metal substrates, using these experimental methods it should be possible to synthesize first-row transition metal silicates films with smaller transition metal ions (considering the relatively large size of the Ti atom) with a judicious choice of substrate. The resulting transition metal silicates resemble crystal structures of naturally existing sheet silicates (phyllosilicates), particularly that of dehydroxylated nontronite, $M_2Si_2O_8$ [17,25] as in Fig. 1(a). The competing bilayer SiO_2 would be composed of a six-membered ring of SiO_4 tetrahedra with out-of-plane mirror symmetry. In the nontronite case, however, the transition metal polyhedra still form six-membered rings, but they are rotated in such a way that all the polyhedra are fivefold-coordinated. In nontronite, therefore, the rings of metal polyhedra have four edge-sharing and two corner-sharing connections.

Even though nontronite-like 2D transition metal silicates are synthesized on metal substrates, it is possible that closely related crystals, such as kaolinite [26] and lizardite [27], which are also phyllosilicates, can also coexist under similar thermodynamic conditions. Kaolinite and lizardite have the chemical formulas $Al_2Si_2O_9H_4$ and $Mg_3Si_2O_9H_4$, hence their dehydroxylated forms are $Al_2Si_2O_9$ and $Mg_3Si_2O_9$, as shown in Figs. 1(b) and 1(c) and Figs. 1(e) and 1(f), respectively. It is known that transition metal atoms such as Fe, Ni, and Co can almost fully substitute Al and Mg in these crystals and similar phyllosilicates [28–33]. Greenalite $[(Fe^{2+}, Fe^{3+})_{2-3}Si_2O_9H_4]$ [34] and nepouite/pecoraite $(Ni_3Si_2O_9H_4)$ [35,36] crystals correspond to the Fe- and Ni-substituted kaolinite and lizardite. Magnetic properties of greenalite were previously studied, and *intrasheet* ferromagnetic order was observed [37]. It was argued that 90° Fe^{2+}-O-Fe^{2+} interactions lead to net magnetization in the 2D layer [37]. Therefore, there is a large chemical space to be explored that could be engineered for 2D ferromagnetism. Additionally, the crystalline space

*sohrab.ismail-beigi@yale.edu

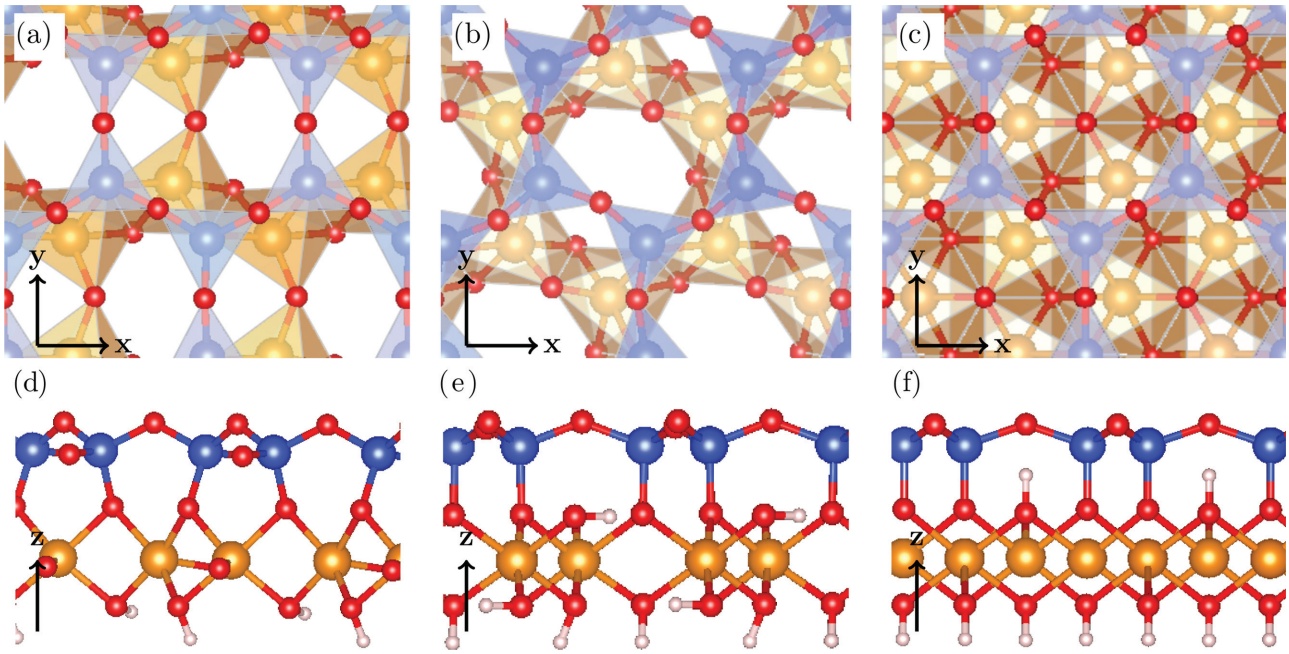

FIG. 1. Top view of the structural templates of the isolated 2D silicate layers studied in this work: (a) nontronite-like, (b) kaolinite-like, and (c) lizardite-like transition metal silicates. Respective side views are indicated in (d), (e), and (f). Blue, red, and orange indicate Si, O, and transition metal atom sites, respectively. Blue polyhedra highlight Si-O polyhedra, and gold polyhedra surround the transition metals. In side images, hydrogen atoms are indicated in white for the highest hydrogenation possible in their respective structures.

groups of kaolinite and lizardite break inversion symmetry, thus these compounds are automatically piezoactive [38].

In this work, we used density functional theory with Hubbard-U correction (DFT+U) to study structural, energetic, magnetic, electronic, and piezoelectric properties of 2D transition metal silicates. We have studied the derivatives of nontronite $M_2Si_2O_8H_x$, kaolinite $M_2Si_2O_9H_x$, and lizardite $M_3Si_2O_9H_x$ as isolated 2D layers in vacuum at various degrees of hydrogenation, where M = Cr, Mn, Fe, Co, and Ni, and $x = 0$–4 ($x = 0$–2 for nontronites). Each transition metal derivative is investigated systematically. For each compound, we report oxidation states of the transition metals, formation and hull energies, energy differences between antiferromagnetic and ferromagnetic phases, and average magnetic moments. Additional data describe the stability regions for compounds that are on the convex hull as well as Gibbs free energies of hydrogenation. Finally, piezoelectric properties are reported for the thermodynamically stable and some metastable layers. We find that there is a rich chemical space for transition metal silicates that are thermodynamically stable with finite piezoelectricity and potential for a magnetic phase with net magnetization.

II. METHODS

All DFT calculations were performed using the Vienna ab initio Simulation Package (VASP) [39,40], using the Perdew-Burke-Ernzerhof (PBE) [41] exchange-correlation functional along with the Hubbard-U approach (PBE+U) [42]. We employ U values of 3.7 eV for Cr, 3.9 eV for Mn, 5.3 eV for Fe, 3.32 eV for Co, and 6.2 eV for Ni for all transition metal oxides using the guidelines in Materials Genome Project [43,44]. These U values were determined according to their accuracy in reproducing the formation energies of all known binary metal oxides [43]. Elemental compounds, whose energies are needed for constructing phase diagrams, are calculated using PBE. PBE and PBE+U energies are combined using an established mixing scheme calibrated using binary oxide formation energies [43]: the PBE and PBE+U mixing scheme provides compositional correction parameters for each atom. Similar composition-based corrections are widely used to correct DFT energies to construct phase diagrams [45,46].

To construct the phase diagrams, we use a procedure based on prior work by Persson *et al.* [47]. To determine the chemical potentials of any compound i under standard conditions, μ_i^0, we define reference chemical potentials, μ_{ref}^0, such that $\mu_i^0 = g_i^0 - \mu_i^{\text{ref}}$, where g_i^0 is the Gibbs free energy of the species i under standard conditions. Gibbs free energy is defined as $g_i^0 = h_i^0 - Ts_i^0$, where h and s are enthalpy and entropy, respectively. Thus, if the reference is at standard conditions, we can simplify as $\mu_i^0 = h_i^0 - h_i^{\text{ref}}$ and here $h_i^{\text{ref}} = E_i^{0,\text{DFT}}$, where $E_i^{0,\text{DFT}}$ is the DFT ground-state energy for the elemental solid. Phase diagrams in this work are constructed using elemental solids, solid oxides, oxygen, hydrogen, and water, which are then used to calculate the relative stabilities of transition metal silicates. Due to the difficulties in treating such a broad range of materials accurately with a single choice of DFT functional, we resort to several practical approximations and empirical corrections to obtain μ_i^{ref} for each compound. For elemental solids, we approximate as $\mu_i^{\text{ref}} \approx E_i^{0,\text{DFT}}$, hence $s_i(T) = 0$. For oxygen gas, however, the reference chemical potential is defined as $\mu_{\text{O}}^{\text{ref}} = E_{\text{O}}^{0,\text{DFT}} + \Delta E_{\text{O}}^{\text{corr}} - Ts_{\text{O}}^{\text{ref}}$, where $\Delta E_{\text{O}}^{\text{corr}}$ is the oxygen gas correction term added to DFT calculations to better reproduce

TABLE I. Average oxidation number of the Fe atoms ($N_{\text{ox}}^{\text{Fe}}$), Fe electronic configuration (EC), calculated formation enthalpies (E_f in eV/at), and energy above the convex hull (E_{hull} in eV/at) for the 2D iron silicates studied in this work. Average magnetic moment per Fe atom (μ_M in μ_B/at) in the high-spin FM state is provided. Compositions on the hull of the phase diagram are in bold font.

Material	$N_{\text{ox}}^{\text{Fe}}$	EC	E_f	E_{hull}	μ_M
Nontronites					
$Fe_2Si_2O_8$	4+	d^4	−2.253	0.175	2.19
$Fe_2Si_2O_8H$	3.5+	d^4, d^5	−2.236	0.122	2.56
$Fe_2Si_2O_8H_2$	3+	d^5	−2.220	0.078	2.96
Kaolinites					
$Fe_2Si_2O_9$	5+	d^3	−2.023	0.218	3.53
$Fe_2Si_2O_9H$	4.5+	d^3, d^4	−2.027	0.163	3.82
$Fe_2Si_2O_9H_2$	4+	d^4	−2.039	0.106	3.87
$Fe_2Si_2O_9H_3$	3.5+	d^4, d^5	−2.037	0.054	4.08
$Fe_2Si_2O_9H_4$	3+	d^5	−2.042	0.000	4.35
Lizardites					
$Fe_3Si_2O_9$	3.33+	d^4, d^5	−2.327	0.091	4.10
$Fe_3Si_2O_9H$	3+	d^5	−2.292	0.066	4.30
$Fe_3Si_2O_9H_2$	2.67+	d^5, d^6	−2.184	0.050	4.03
$Fe_3Si_2O_9H_3$	2.34+	d^5, d^6	−2.095	0.023	3.93
$Fe_3Si_2O_9H_4$	2+	d^6	−2.015	0.000	3.75

experimental binary oxide formation energies [48]. The reference, "ref," depends here on the pressure/temperature of the gases. We use the entropy $s_{\text{O}}^{\text{ref}}$ from prior work [49]. For a binary solid oxide, A_xO_y, like the elemental solids, we approximate the entropic terms as negligible [47] and write the chemical potential for that compound as $\mu^0_{A_xO_y} = E^{\text{DFT}}_{A_xO_y} - x\mu^{\text{ref}}_A - y\mu^{\text{ref}}_{\text{O}}$. Water is a particularly difficult case for most theoretical methods. Therefore, we use the free energy of formation of H_2O at room temperature, $\mu^0_{H_2O} = -2.46\,\text{eV/H}_2\text{O}$. The hydrogen chemical potential depends on the chemical potential of H_2O and O, hence it is obtained indirectly as follows. Using the water formation reaction, we define $\mu^{\text{ref}}_{\text{H}} = 1/2[g^{\text{ref}}_{H_2O} - \mu^{\text{ref}}_{\text{O}} - \mu^0_{H_2O}]$. Here, $g^{\text{ref}}_{H_2O} = E^{0,\text{DFT}}_{H_2O} - Ts^0_{H_2O}$. Numerical values for the variables discussed here are provided in the Supplemental Material along with a more detailed explanation and examples.

We calculate elastic tensor coefficients, C_{ij}, with no ionic relaxations, using the finite differences method and the strain coefficients of the piezoelectric tensor, e_{ij}, via the Berry phase method [50,51] in VASP. An orthogonal supercell was used to calculate the elastic and piezoelectric constants. A Γ-centered reciprocal space grid of $4 \times 8 \times 1$ (corresponding to a grid density of 120 Å^{-3}) for sampling the first Brillouin zone and an energy cutoff of 520 eV are used in all our calculations. We ensured a spacing of a minimum 30 Å of vacuum between the periodic images of layers in all calculations. Dipole corrections [52] were also included along the out-of-plane direction to reduce spurious interactions between periodic images.

III. RESULTS AND DISCUSSION

Using the phase diagram generation procedure described in Sec. II, we study the stabilities of all the transition metal silicates (from Cr to Ni) shown in Fig. 1 at varying hydrogenation levels. We consider three structural templates for these transition metal silicates. These templates are based on natural minerals or are ones that have been synthesized. These are nontronite-like silicates $M_2Si_2O_8H_n$, where $n = 0$–2, kaolinite-like silicates $M_2Si_2O_9H_n$, where $n = 0$–4, and lizardite-like silicates $M_3Si_2O_9H_n$, where $n = 0 - 4$. For any hydrogenation level, n, all possible combinations of hydrogen bindings to the binding sites were considered, and the minimum energy structure is reported. In Figs. 1(d)–1(f), these structures are shown with the highest degree of hydroxylation possible. Kaolinite has two additional oxygens compared to nontronite, and all transition metal polyhedra in kaolinite are sixfold-coordinated and edge-sharing. Lizardite, on the other hand, has one additional metal atom compared to kaolinite, which makes the metal oxide layer triangular, as opposed to the honeycomb lattice in kaolinite. Once the structural stabilities are explained (Sec. III A), we describe other computed physical properties (remaining sections).

A. Thermodynamic stabilities

1. Fe silicates

In Table I, we show the average oxidation number, transition metal electronic configuration, formation and hull energies, and average Fe magnetic moments for all the Fe silicates studied. Average oxidation numbers, N_{ox}, are determined by assuming O and Si to be closed shell ions (i.e., O^{2-} and Si^{4+} ions). The N_{ox} can be used with the transition metal electronic configuration (EC) to show that a charge ordered structure is found. EC was determined by using the magnetic moment on the transition metal atoms and also chemical intuition. For example, for $Fe_3Si_2O_9$ with $N_{\text{ox}} = 3.33+$ and EC of d^4, d^5 indicates that one of the Fe atoms is d^4 (4+) and the other two are d^5 (3+). We find that this structure is monoclinic (Cm, no. 8) with $\gamma = 119.64°$. However, when the same structure is forced to have trigonal symmetry ($P31m$, no. 157), the energy is increased by 0.05 eV/f.u., and all three Fe atoms become magnetically identical (as expected when constrained to be magnetically collinear). Similar symmetry breaking and charge disproportionation is observed in all structures with noninteger N_{ox} in Table I. Structural parameters of all the

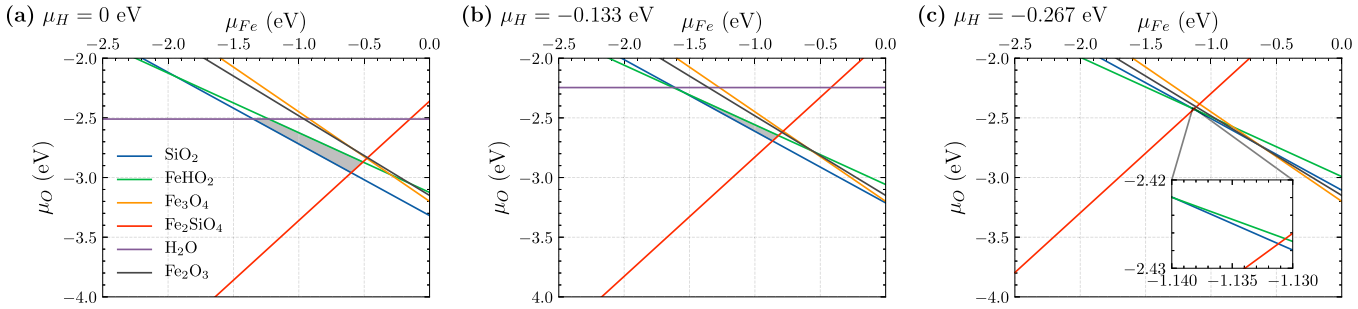

FIG. 2. Phase diagrams for 2D $Fe_3Si_2O_9H_4$ with (a) hydrogen chemical potential μ_H is set to 0 eV, (b) $\mu_H = -0.133$ eV, and (c) $\mu_H = -0.267$ eV. Stability regions of $Fe_3Si_2O_9H_4$ are shaded in gray. In (c) the shaded area is given in the inset for further detail.

2D materials are given in the Supplementary Information (SI) [53].

The convex hull energies, E_{hull}, in Table I are determined using a Fe-Si-O-H quaternary phase diagram [53]. The only compounds that have zero hull energy in Table I are $Fe_2Si_2O_9H_4$ and $Fe_3Si_2O_9H_4$. Although Fe-nontronites were shown to exist [17] on Ru (111) substrate, Table I shows that this phase is unstable in isolation even when it is fully hydrogenated. Nevertheless, in all the compounds, there is a clear trend of decreasing hull energy with hydroxylation. However, it is possible that metastable compounds (e.g., $E_{\text{hull}} < 50$ meV/at) can be kinetically trapped making them experimentally accessible. In the literature, a tolerance on the DFT hull energies of around 10 meV/at is used to eliminate false negatives on the convex hull [54]. However, the smallest nonzero hull energy in Table I is 23 meV/at, which is well above this likely tolerance of DFT error.

In Fig. 2, we show the chemical stability ranges for $Fe_3Si_2O_9H_4$ as a function of the O and Fe chemical potentials, μ_O and μ_{Fe}. We assume that our quaternary compound (here $Fe_3Si_2O_9H_4$) is in equilibrium with the reservoirs, so that there are three independent chemical potentials. We choose μ_{Fe} and μ_O as the two independent parameters for our study, and we fix the third, μ_H, at various values to understand how the stability regions are modified. Three different μ_H values are selected based on the maximum, average, and minimum μ_H where $Fe_3Si_2O_9H_4$ can exist based on the calculated phase diagram. In general, a "facet" of the phase diagram using the convex hull formalism indicates a hull member, or in other words, it means an $(N-1)$-dimensional geometric domain on the convex hull where there is a set of compounds that can coexist in equilibrium. Here, N is the number of compounds used to construct the phase diagram. In a binary convex hull phase diagram, for example, there are two compounds, hence the dimension of a facet would be 1. In this case, the facet has a special name called a tie-line, and each tie-line connects two points on the phase diagram which coexist on this tie-line. For a quaternary compound, such as $Fe_3Si_2O_9H_4$, a facet is then a three-dimensional object which is formed by connecting four points in the convex hull phase diagram. These four points correspond to four compounds that coexist within the three-dimensional convex hull facet. All the facets of the quaternary phase diagram where $Fe_3Si_2O_9H_4$ is found to be thermodynamically stable are given in the SI [53]. For example, $\mu_H = 0$ eV is possible on a facet, where $Fe_3Si_2O_9H_4$-H_2-SiO_2-H_2O can coexist. However, $\mu_H = -0.267$ eV is obtained from the $Fe_3Si_2O_9H_4$-Fe_2SiO_4-$FeHO_2$-SiO_2 facet (coexistence region). Therefore, the stability of $Fe_3Si_2O_9H_4$ is bounded by $0 > \mu_H > -0.267$ eV. With μ_H fixed in Figs. 2 and 3, the H_2O coexistence curves in Fig. 2 are always horizontal. In Fig. 3, we perform the same analysis on $Fe_3Si_2O_9H_4$ and find that the stability region, where no other phase precipitates, is much smaller in all cases compared to Fig. 2.

There are various trends that can guide experimental synthesis. Decreasing the hydrogen chemical potential yields a smaller stability region, hence hydrogen-rich environments should more easily yield $Fe_3Si_2O_9H_4$. Next, we find that the stability region of $Fe_3Si_2O_9H_4$ is mainly controlled by competition of SiO_2 and $FeHO_2$ formation. In addition, phase separation into binary oxides is not relevant. Next, under fixed μ_O, increasing the μ_{Fe} will lead to precipitation of $FeHO_2$, and decreasing μ_{Fe} (increasing μ_{Si}) will lead to precipitation of SiO_2. Under fixed μ_{Fe}, increasing μ_O (decreasing μ_{Si}) will generally lead to the formation of $FeHO_2$. In Fig. 2(a), there is a small region near $\mu_{Fe} < -1.3$ eV, where increased μ_O will first lead to precipitation of H_2O and then $FeHO_2$ will follow.

We compare the stability curves of $Fe_2Si_2O_9H_4$ in Fig. 3 to the stability curves of $Fe_3Si_2O_9H_4$ in Fig. 2. Our main finding is that the stability region is much smaller compared to Fig. 2. In Fig. 3(a), for example, it is a very small region around $\mu_{Fe} = -1.5$ eV and $\mu_O = -2.3$ eV. We believe the rather small sizes of the stable regions in both figures are primarily due to the fact that both $Fe_3Si_2O_9H_4$ and $Fe_2Si_2O_9H_4$ are isolated 2D layers, but their energetics are competing against bulk compounds. The iron silicate can be further stabilized trivially by considering its bulk version, but more relevantly by placing it on a substrate for added stabilization from the wetting (binding) energy to the substrate.

For example, in Fig. 2, such an added binding energy would increase the stability region as the SiO_2 and Fe_2SiO_4 curves would shift down with the increased formation energy of the $Fe_3Si_2O_9H_4$ while the curves for all the other iron oxides and $FeHO_2$ remain fixed at constant μ_H. The same effect must also occur for $Fe_2Si_2O_9H_4$ given the fact that the SiO_2 curve will shift down as a result.

In Figs. 4 and 5, we show the Gibbs free energy of hydrogenation for the following chemical reaction:

$$M_xSi_2O_9 + \frac{n}{2}H2 \longrightarrow M_xSi_2O_9H_n. \quad (1)$$

We note that these curves only indicate the relative stability of each compound, not the thermodynamic stability of

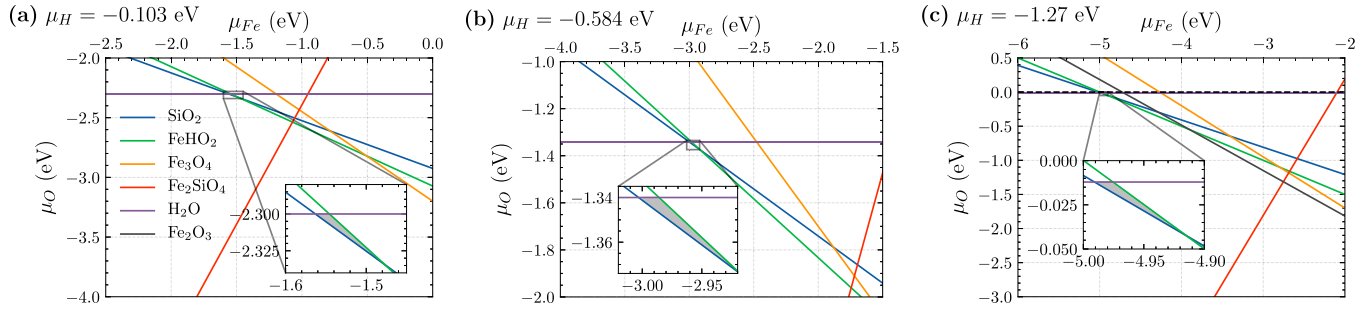

FIG. 3. Phase diagrams for $Fe_2Si_2O_9H_4$: (a) hydrogen chemical potential μ_H is set to -0.103 eV, (b) μ_H is set to -0.584 eV, and (c) μ_H is set to -1.27 eV. Stability regions are shaded in gray. Insets show the shaded regions in greater detail.

the compound which is determined through hull energies in Table I. Equation (1) only describes whether hydrogenation of the transition metal silicates is thermodynamically favorable.

Among the hydroxylated phases of $Fe_3Si_2O_9H_n$, only $Fe_3Si_2O_9H$ and $Fe_3Si_2O_9H_4$ are relatively stable compared to the others, which can be explained through the valence state of the Fe atoms. In $Fe_3Si_2O_9H$, all the Fe atoms are in the 3+ state, whereas in $Fe_3Si_2O_9H_4$ all the Fe atoms are in the 2+ state. Hence, we can conclude that under increasingly H-rich conditions, the charge disproportionation of the Fe atoms is expected to disappear.

In Fig. 5, we show the same analysis for $Fe_2Si_2O_9H_n$, and we find that, essentially, a transition only occurs between $Fe_2Si_2O_9$ and $Fe_2Si_2O_9H_4$ compounds. This can be understood in a similar way as in (4). In $Fe_2Si_2O_9$, all Fe atoms are in the 5+ state, and in $Fe_2Si_2O_9H_4$ they reduce to the 3+ state. Given that Fe would prefer oxidation states with 2+ and 3+, there is no intermediate hydrogenated compound that is stable. Additionally, in Fig. 5, the transition occurs at a similar chemical potential to the first transition in Fig. 4, but much lower than the second transition in Fig. 4 where complete hydrogenation has occurred. This implies that it is significantly easier to obtain a completely hydrogenated 2D Fe silicate with the kaolinite-like structure once the base compound is formed.

Separately, we calculate the cleavage energy of 2D Fe silicates to show that these 2D materials are exfoliable assuming that their bulk counterparts can be synthesized. For Fe kaolinite, we find the cleavage energy to be 14 meV/Å^2, while for Fe lizardites the cleavage energy is 18 meV/Å^2. According to the large-scale screening studies of the exfoliation energies of 2D compounds [55], exfoliation energies below 30–35 meV/Å^2 are classified as an "easily exfoliable" regime, meaning that it can be exfoliated using simple techniques such as mechanical exfoliation. For the rest of the transition metal silicates, we provide these numbers in the SI [53], but overall they are between 18 and 22 meV/Å^2 for lizardites and between 14 and 18 meV/Å^2 for kaolinites, showing that the transition metal only has a negligible effect on the cleavage energies.

2. Cr silicates

Our analysis of Cr silicates and the remaining silicates will follow closely our analysis of Fe silicates. In Table II, we present our data on Cr silicates in the same manner as the Fe silicates in Table I. Hull energies in Table II are determined using a Cr-Si-O-H quaternary phase diagram using the compounds listed in the Supplementary Information [53]. The only stable compound in Table II is $Cr_2Si_2O_9H_4$. There is a clear trend of increasing stability with increased hydrogenation in nontronites and kaolinites, but for lizardites the trend

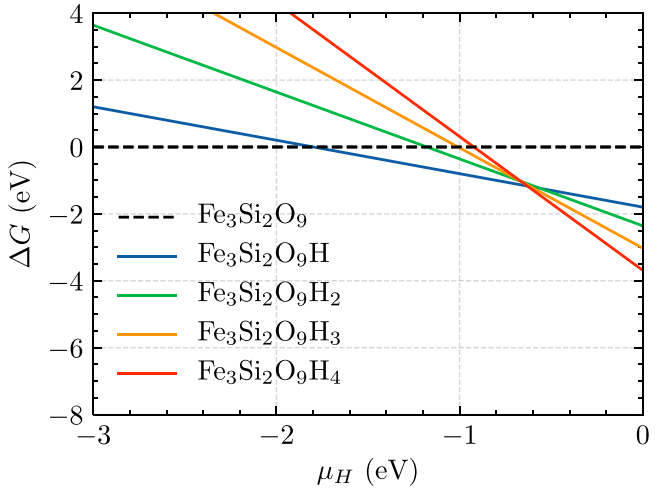

FIG. 4. Gibbs free energy, ΔG, of the hydrogenation reaction of Eq. (1) for $Fe_3Si_2O_9H_n$ as a function of the chemical potential of hydrogen, μ_H.

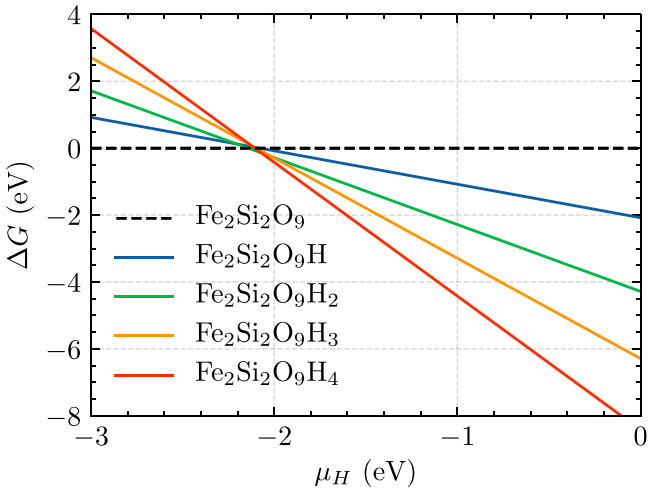

FIG. 5. Gibbs free energy, ΔG, for Eq. (1) and $Fe_2Si_2O_9H_n$ as a function of the chemical potential of hydrogen.

TABLE II. Ground-state properties of 2D Cr silicates.

Material	N_{ox}^{Cr}	EC	E_f	E_{hull}	μ_M
Nontronites					
$Cr_2Si_2O_8$	4+	d^2	−2.553	0.057	2.19
$Cr_2Si_2O_8H$	3.5+	d^2, d^3	−2.428	0.113	2.55
$Cr_2Si_2O_8H_2$	3+	d^3	−2.312	0.17	2.96
Kaolinites					
$Cr_2Si_2O_9$	5+	d^1	−2.368	0.041	1.43
$Cr_2Si_2O_9H$	4.5+	d^1, d^2	−2.315	0.045	1.94
$Cr_2Si_2O_9H_2$	4+	d^2	−2.280	0.036	2.32
$Cr_2Si_2O_9H_3$	4.5+	d^2, d^3	−2.235	0.019	2.71
$Cr_2Si_2O_9H_4$	3+	d^3	−2.201	0	2.96
Lizardites					
$Cr_3Si_2O_9$	3.33+	d^2, d^3	−2.621	0.032	2.83
$Cr_3Si_2O_9H$	3+	d^3	−2.545	0.046	2.98
$Cr_3Si_2O_9H_2$	2.67+	d^3, d^4	−2.346	0.083	3.36
$Cr_3Si_2O_9H_3$	2.34+	d^3, d^4	−2.170	0.116	3.68
$Cr_3Si_2O_9H_4$	2+	d^4	−2.027	0.132	3.75

is in the opposite direction. This may be because, in lizardites, increased hydrogenation yields the 2+ charge state Cr, which is energetically unfavorable compared to the 3+ state. This agree with the fact that Cr^{3+} compounds are more common than Cr^{2+} compounds [56].

The stability diagram for $Cr_2Si_2O_9H_4$ is provided in the Supplementary Information. Similar to $Fe_2Si_2O_9H_4$ in Fig. 3, the stability region of $Cr_2Si_2O_9H_4$ is bounded by H_2O, SiO_2, and $CrHO_2$. When constructing the Cr-Si-O-H phase diagram, our search did not yield a thermodynamically stable Cr-Si-O ternary compound, unlike Fe_2SiO_4. The corresponding Cr_2SiO_4 structure has been synthesized only at elevated temperatures with rapid quenching [57], and it is reported to be metastable within DFT [58], suggesting that the structure can only be kinetically trapped. We find that the Gibbs free energy of hydrogenation of $Cr_2Si_2O_9H_4$, given in the Supplementary Information, is similar to the hydrogenation of $Fe_2Si_2O_9H_4$ in Fig. 5. The main difference between the hydrogenation of two materials is that the energetic crossing between $Cr_2Si_2O_9$ and $Cr_2Si_2O_9H_4$ occurs at a larger chemical potential compared to $Fe_2Si_2O_9H_4$. This agrees with the fact that Fe has a larger ionization potential compared to Cr, hence hydrogenation is comparatively more favorable at lower hydrogen availability.

3. Mn silicates

Table III shows that none of the Mn silicates are found to be stable in the Mn-Si-O-H phase diagram we constructed using the compounds given in the Supplementary Information. Nevertheless, trends are observed similar to those in Cr and Fe silicates, such that increased hydrogenation typically stabilizes the compound. This trend is more obvious in $Mn_2Si_2O_9H_n$, where Mn transitions from being 5+ to 3+ with increased hydrogenation. However, for $Mn_3Si_2O_9H_n$, cases where Mn has an integer oxidation state of 3+ or 2+ are more stable compared to fractional oxidation states. We find that $Mn_3Si_2O_9H_n$ favors the 3+ oxidation state only slightly more than the 2+ state, which is expected given that these two oxidation states are the most commonly observed for Mn compounds [56].

We studied the hydrogenation of Mn silicates using Eq. (1), and we show the associated figures in the Supplementary Information. We find the same relation between the Gibbs free energy of hydrogenation in $Mn_3Si_2O_9H_n$ and $Fe_3Si_2O_9H_n$ in Fig. 4. The only difference is that the hydrogen chemical potentials at the transition points for $Mn_3Si_2O_9H_n$ are higher compared to $Fe_3Si_2O_9H_n$, which is a similar trend to what we noted for Cr silicates. For $Mn_2Si_2O_9H_n$, however, there is an additional region of hydrogen chemical potential where $Mn_3Si_2O_9H$ and $Mn_3Si_2O_9H_2$ are stable as well. This is in contrast to the Fe silicates, where we have a direct transition from $Fe_3Si_2O_9$ to $Fe_3Si_2O_9H_4$ in Fig. 5. This may be because Mn tends to commonly accept a wider range of oxidation states compared to Fe, therefore the differences between higher degrees of ionization energies should be small enough to allow stepwise hydrogenation as opposed to the Fe-silicate examples.

4. Co silicates

Table IV shows that the stability trends for Co silicates are very similar to those in Table I. Again, the stability increases with increased hydrogenation, and hull energies of trioctahedral Co silicates are consistently smaller than dioctahedral derivatives. Similarly, we find that the stability regions of $Co_3Si_2O_9H_4$ are larger than $Co_2Si_2O_9H_4$ (see the Supplementary Information). An important difference between the Co and Fe silicates is that $Co_2Si_2O_9H_4$ starts forming at a lower hydrogen chemical potential than for $Fe_{(2,3)}Si_2O_9H_4$ silicates. Given that the stability region is mainly determined by SiO_2, $CoHO_2$, and H_2O curves, this can be explained by the fact that the $CoHO_2$ formation enthalpy is significantly higher than $FeHO_2$ (1.13 versus 1.56 eV). Compared to $FeHO_2$, $CoHO_2$ is less likely to form.

We studied the hydrogenation of Co silicates using Eq. (1), and we show the plots in the Supplementary Information. In $Co_3Si_2O_9H_4$, we find that the Gibbs free energy of hydrogenation has the following trend going from Fe to Mn and Co. In $Fe_3Si_2O_9H_n$ (Fig. 4), the hydrogenation is stepwise such that after $Fe_3Si_2O_9$, first $Fe_3Si_2O_9H$ and then $Fe_3Si_2O_9H_4$

TABLE III. Ground-state properties of 2D Mn silicates.

Material	N_{ox}^{Mn}	EC	E_f	E_{hull}	μ_M
Nontronites					
$Mn_2Si_2O_8$	4+	d^3	−2.375	0.172	3.28
$Mn_2Si_2O_8H$	3.5+	d^2, d^3	−2.317	0.125	3.51
$Mn_2Si_2O_8H_2$	3+	d^4	−2.256	0.095	3.85
Kaolinites					
$Mn_2Si_2O_9$	5+	d^2	−2.122	0.169	3.02
$Mn_2Si_2O_9H$	4.5+	d^2, d^3	−2.158	0.114	3.06
$Mn_2Si_2O_9H_2$	4+	d^3	−2.172	0.032	3.16
$Mn_2Si_2O_9H_3$	3.5+	d^3, d^4	−2.126	0.018	3.54
$Mn_2Si_2O_9H_4$	3+	d^4	−2.069	0.013	3.87
Lizardites					
$Mn_3Si_2O_9$	3.33+	d^3, d^4	−2.467	0.038	3.92
$Mn_3Si_2O_9H$	3+	d^4	−2.391	0.026	3.93
$Mn_3Si_2O_9H_2$	2.67+	d^4, d^5	−2.274	0.046	4.27
$Mn_3Si_2O_9H_3$	2.34+	d^4, d^5	−2.168	0.045	4.44
$Mn_3Si_2O_9H_4$	2+	d^5	−2.088	0.031	4.63

is formed. $Mn_3Si_2O_9H_4$ is similar to this, but the range of stability for $Mn_3Si_2O_9H$ is smaller compared to $Fe_3Si_2O_9H$. Following this trend, the range of stability for $Co_3Si_2O_9H$ disappears completely (we will see that the range of stability for $Ni_3Si_2O_9H$ is again smaller compared to $Fe_3Si_2O_9H$ and $Mn_3Si_2O_9H$). Gibbs free energy of hydrogenation curves for $Co_2Si_2O_9H_n$ are similar to $Fe_2Si_2O_9H_n$ except that the μ_H at the transition point for $Co_2Si_2O_9H_n$ is slightly smaller.

5. Ni silicates

In Table V we observe stability trends that are very similar to Table I. Again, the stability increases with increased hydrogenation, and hull energies of trioctahedral Ni silicates are consistently smaller than dioctahedral derivatives. However, the hull energy of $Ni_2Si_2O_9$ is larger compared to $Fe_2Si_2O_9$, whereas the hull energy of $Ni_3Si_2O_9$ is smaller than $Fe_3Si_2O_9$. This indicates that overall, Ni silicates have a stronger tendency to form trioctahedral compounds compared to Fe silicates. This is to be expected: Ni commonly has an oxidation state of 2+, unlike Mn, Fe, and Co, which are more commonly found in 2+ and 3+ oxidation states. Similarly, we have found that the only stable Cr silicate in our work is $Cr_2Si_2O_9H_4$, where Cr has an oxidation state of 3+ in the dioctahedral form. In $Ni_3Si_2O_9H_4$, Ni prefers an oxidation state of 2+ in the trioctahedral form. Hence, it can be argued that for Mn-Co silicates, dioctahedral and trioctahedral phases are in competition and coexist, but for Cr and Ni silicates one phase is clearly favored over the other.

We studied the hydrogenation of Ni silicates using Eq. (1), and we show the data in the Supplementary Information. Hydrogenation of $Ni_3Si_2O_9H_n$ follows the same trend that we discussed in $Co_3Si_2O_9H_n$. There is a stability range for $Ni_3Si_2O_9H$ that exists, but it is much smaller compared to $Mn_3Si_2O_9H$ and $Fe_3Si_2O_9H$.

TABLE IV. Ground-state properties of 2D Co silicates.

Material	N_{ox}^{Co}	EC	E_f	E_{hull}	μ_M
Nontronites					
$Co_2Si_2O_8$	4+	d^5	−2.078	0.091	2.52
$Co_2Si_2O_8H$	3.5+	d^6, d^5	−2.059	0.049	2.68
$Co_2Si_2O_8H_2$	3+	d^6	−2.028	0.028	3.11
Kaolinites					
$Co_2Si_2O_9$	5+	d^4	−1.924	0.078	2.58
$Co_2Si_2O_9H$	4.5+	d^4, d^5	−1.865	0.092	2.25
$Co_2Si_2O_9H_2$	4+	d^5	−1.868	0.050	2.05
$Co_2Si_2O_9H_3$	3.5+	d^5, d^6	−1.861	0.020	2.78
$Co_2Si_2O_9H_4$	3+	d^6	−1.847	0.000	3.15
Lizardites					
$Co_3Si_2O_9$	3.33+	d^5	−2.049	0.036	2.07
$Co_3Si_2O_9H$	3+	d^5, d^6	−2.003	0.036	3.01
$Co_3Si_2O_9H_2$	2.67+	d^6	−1.958	0.033	2.99
$Co_3Si_2O_9H_3$	2.34+	d^6, d^7	−1.932	0.010	2.87
$Co_3Si_2O_9H_4$	2+	d^7	−1.899	0.000	2.74

TABLE V. Ground-state properties of 2D Ni silicates.

Material	N_{ox}^{Ni}	EC	E_f	E_{hull}	μ_M
Nontronites					
$Ni_2Si_2O_8$	4+	d^6	−1.709	0.256	1.55
$Ni_2Si_2O_8H$	3.5+	d^6, d^7	−1.761	0.187	1.56
$Ni_2Si_2O_8H_2$	3+	d^7	−1.797	0.135	1.47
Kaolinites					
$Ni_2Si_2O_9$	5+	d^5	−1.511	0.304	1.29
$Ni_2Si_2O_9H$	4.5+	d^5, d^6	−1.579	0.264	1.61
$Ni_2Si_2O_9H_2$	4+	d^6	−1.571	0.232	2.12
$Ni_2Si_2O_9H_3$	3.5+	d^6, d^7	−1.671	0.170	2.14
$Ni_2Si_2O_9H_4$	3+	d^7	−1.647	0.110	2.16
Lizardites					
$Ni_3Si_2O_9$	3.33+	d^6, d^7	−1.756	0.069	1.33
$Ni_3Si_2O_9H$	3+	d^7	−1.788	0.030	1.40
$Ni_3Si_2O_9H_2$	2.67+	d^7, d^8	−1.792	0.021	1.54
$Ni_3Si_2O_9H_3$	2.34+	d^7, d^8	−1.774	0.034	1.66
$Ni_3Si_2O_9H_4$	2+	d^8	−1.804	0.000	1.80

6. *Structural stability of kaolinites and lizardites*

It is known that the parent compounds of kaolinite—$Al_2Si_2O_9H_4$ and $Mg_3Si_2O_9H_4$—exist naturally [26,27], but our literature search has not yielded any work on theoretical phonon dispersion of these materials. Nevertheless, in order to show that transition metal counterparts of these 2D materials are structurally stable, we calculated the phonon dispersions of $Cr_2Si_2O_9H_4$ and $Mn_3Si_2O_9H_4$ as exemplars. (An exhaustive study of the phonon dispersions of all the metal silicates here is avoided due to high computational costs of performing so many calculations.) While $Mn_3Si_2O_9H_4$ is structurally stable, for $Cr_2Si_2O_9H_4$ we see very weak structural instabilities near Γ. We find that the size and presence of these instabilities depend strongly on numerical parameters such as the size of the supercell or the force-constant cutoff radius, indicating that they are numerical artifacts. A detailed discussion is provided in the SI [53]. Our conclusion is that these 2D silicates are structurally stable.

B. Magnetic structure

To better understand the magnetic structures, we begin with the geometry of the silicates starting with the kaolinites. In Fig. 6, we show that the kaolinites have a distorted honeycomb lattice. This distortion yields quasi-1D structures having equidistant transition metal (TM) atoms along 1D zigzag chains and a different TM-TM distance perpendicular to the zigzag chains. This is because the $[SiO_4]^{-2}$ layer modulates the O ligands such that they breaks the hexagonal symmetry of the transition metal oxide layer. For example, each Cr atom in $Cr_2Si_2O_9H_4$ has three Cr neighbors, with two of them $d(\text{Cr-Cr})_1 = 3.072$ Å away (black lines in Fig. 6) and one $d(\text{Cr-Cr})_2 = 3.012$ Å away (red lines in Fig. 6). This pattern of bond lengths is important to consider when comparing to other compounds such as MnX_3 [59], where the Mn also has a d^4 electronic state similar to $Mn_2Si_2O_9H_4$. In this work, we aim to screen whether there are any antiferromagnetic (AFM) phases which are energetically more favorable than the ferromagnetic (FM) phase. To understand the magnetic interactions between transition atoms with bond length alternations, such as $d(\text{Cr-Cr})_{1,2}$, larger supercells should be considered in future work.

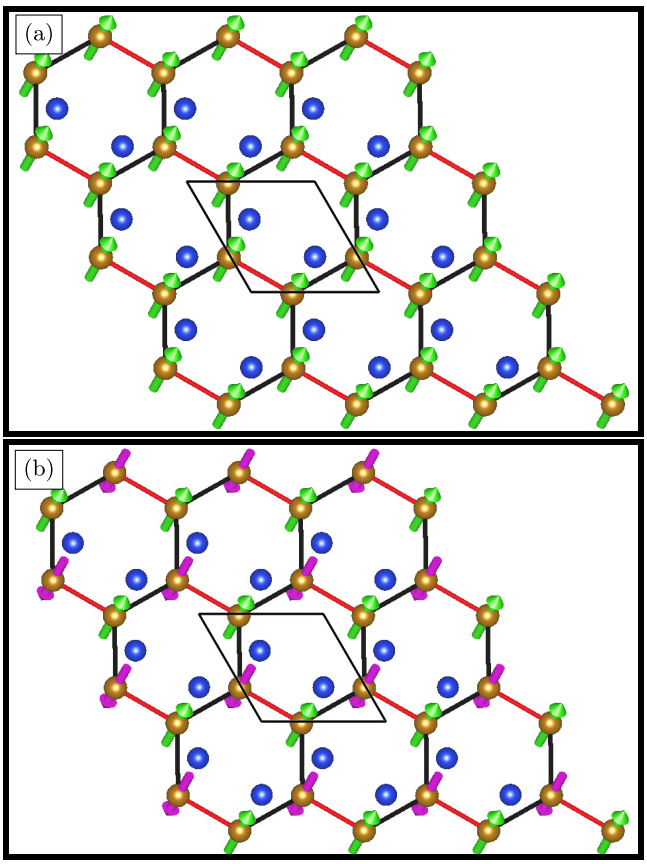

FIG. 6. (a) FM and (b) G-AFM ordering considered for kaolinite structures. O and H atoms are omitted for clarity; only the transition metal (TM) atoms and Si are shown in gold and blue, respectively. Up and down spin directions are shown with green and magenta arrows, respectively. Distortions from the perfect honeycomb lattice are displayed also: longer TM bonds are shown in black, and shorter TM bonds are shown in red. The primitive cell of the structure is shown with black lines at the center of each figure.

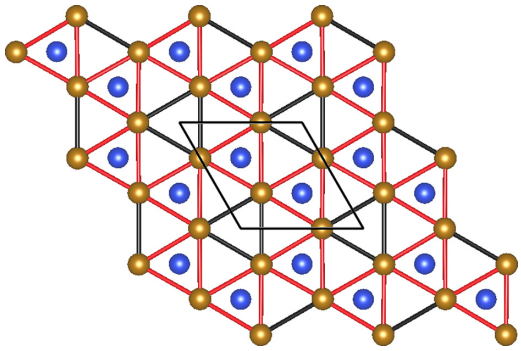

FIG. 7. Distortion of the triangular lattice in lizardites. Gold spheres show the TM atoms, blue spheres show Si atoms. O and H are omitted for clarity. Longer TM-TM bonds are shown using black, whereas the shorter TM-TM bonds are shown using red lines. The primitive cell of the structure is indicated using black lines in the center of the figure.

In lizardites, a similar distortion as in the kaolinites is found. A prototype of a lizardite structure is shown in Fig. 7. For example, each Fe atom in $Fe_3Si_2O_9H_4$ has six Fe neighbors, where any Fe has four Fe neighbors with $d(\text{Fe-Fe})_1 = 3.14$ Å (red lines in Fig. 7) and two Fe neighbors with $d(\text{Fe-Fe})_2 = 3.19$ Å (black lines in Fig. 7). This is because the Si-O layer modulates the transition metal oxide layer. Each Si-tetrahedron is centered on top of an equilateral triangle of Fe-Fe bonds with $d(\text{Fe-Fe})_1$ as can be seen in Fig. 7. As the Si-O layer forms a honeycomb lattice, the site above the equilateral triangles with $d(\text{Fe-Fe})_2$ is empty, hence the Fe-Fe distances are modulated. Non-FM magnetic orderings in the primitive cell of lizardite structure are spin-frustrated. Therefore, we calculate a striped AFM ordering using a rectangular supercell which is simply doubled along one primitive vector. Although even larger supercells will allow for more complex magnetic ordering patterns, here we restrict ourselves to these simple orderings to obtain an overall assessment of the magnetic ordering energy scales at reasonable computational costs. To understand the potential of these structures for 2D FM behavior, comparing simple FM and AFM orderings provides a good estimate of the relative stability.

In Table VI, we compare AFM and FM phases of kaolinites and lizardites.

Our results in Table VI show that the energy differences between the AFM and FM phases are mostly quite small, and

TABLE VI. Magnetic properties of transition metal silicates.

Material	$E_{\text{AFM}} - E_{\text{FM}}$ (meV per metal atom)
Kaolinites	
$Cr_2Si_2O_9H_4$	3
$Mn_2Si_2O_9H_4$	−8
$Fe_2Si_2O_9H_4$	−3
$Co_2Si_2O_9H_4$	−28
$Ni_2Si_2O_9H_4$	−201
Lizardites	
$Mn_3Si_2O_9H_4$	−24
$Fe_3Si_2O_9H_4$	−1
$Co_3Si_2O_9H_4$	1
$Ni_3Si_2O_9H_4$	−2

that the ground state is mainly AFM. For many, the small AFM-FM energy difference means no magnetic ordering is likely at room temperature; for $Co_2Si_2O_9H_4$, $Mn_3Si_2O_9H_4$, and $Ni_2Si_2O_9H_4$, the AFM order is expected to survive at or near room temperature. We note that $Ni_2Si_2O_9H_4$ in Table VI is a thermodynamically unstable structure since each Ni atom has a 3+ oxidation state. Similarly, $Cr_3Si_2O_9H_4$ is also a thermodynamically unstable material, thus Cr atoms would have a 2+ oxidation state in this structure. In the Supplemental Material [53], we show that the same conclusion can also be made for $Cr_3Si_2O_9H_4$.

The main FM candidate in Table VI is the kaolinite $Cr_2Si_2O_9H_4$, although the Curie temperature is likely to be very low. This is similar to the magnetism in Cr-Ni pyroxenes, which yields an AFM ground state for Mn to Fe pyroxenes [60,61] but a FM ground state for Cr pyroxenes. Pyroxenes and kaolinites are structurally rather similar. In both structures, the magnetism is mediated over M-O-M bonds which are close to 90°. In pyroxenes, however, M-O octahedra form one-dimensional chains which are separated by alkali atoms such as Li and Na, as opposed to the two-dimensional M-O layer in kaolinites. In kaolinites, however, the structural modulation seen in Fig. 6 also indicates that the magnetic coupling is not isotropic, hence the situation is similar to the pyroxenes. In Cr pyroxenes, it was shown that the AFM t_{2g}-t_{2g} exchange interaction is nearly compensated by the FM t_{2g}-e_g exchange, but fine-tuning of these interactions is possible via the size of the alkali atom [60]. In $NaCrGe_2O_6$, the largest Cr-Cr separation was observed which yields a FM structure [60]. Although not examined here, future work can examine if it is possible to incorporate additional transition metal atoms in the vacancies of the honeycomb lattice of Cr kaolinite to increase FM coupling and/or have a ferrimagnetic ground state with a net magnetization.

As we previously discussed, greenalite, $Fe_{2,3}Si_2O_9H_4$, is observed to be ferromagnetic in the plane with an intraplane magnetic coupling constant of 15 K [28]. Fe sites in greenalite are disordered, however, meaning that some octahedral sites are filled with Fe, whereas others are hollow. In this perspective, greenalite can be considered a solid solution of the ordered Fe-kaolinite and Fe-lizardite phases we studied. However, our calculations do not yield a ferromagnetic order in these ordered lizardite and kaolinite phases. For Fe silicates, our calculations yield a G-type checkerboard AFM phase for $Fe_2Si_2O_9H_4$ and a striped AFM phase for $Fe_3Si_2O_9H_4$ as energetically more favorable compared to the FM phases. Therefore, we can understand that the ferromagnetism of greenalite is correlated to the disorder in its structure. Similar accounts of enhanced ferromagnetism with increased disorder were reported in 3D alloys [62] as well as disordered and doped 2D materials [63,64]. As we predict both lizardite and kaolinite Fe silicates to be thermodynamically stable, synthesis conditions might be engineered to make partially occupied Fe-O layers, which can yield magnetic properties similar to greenalite.

C. Piezoelectric properties

Here, we describe the piezoelectric properties of the thermodynamically stable 2D silicates identified above. For a material to be piezoelectric, it has to be insulating or

semiconducting plus have broken inversion symmetry. We provide the density of states plots and the band gaps of the kaolinites and lizardites we studied in the SI [53]: the band gaps of the transition metal silicates we studied are all above 1 eV [53]. Both kaolinites and lizardites have symmetry point groups that do not include inversion, hence they are expected to have a finite piezoelectric response under strain or electric field. As the side views of Figs. 1(d)–1(f) show, the Si-O and transition metal-O layers are chemically stacked, and the resulting dipole is in the z-direction. We use the following standard relations to calculate the elastic modulus tensor C_{ij} and piezoelectric strain tensor $e_{\alpha j}$:

$$\begin{aligned} C_{ij} &= \frac{d\sigma_i}{d\eta_j}, \\ e_{\alpha j} &= \frac{dP_\alpha}{d\eta_j} = e_{\alpha j,c} + e_{\alpha j,i}, \\ e_{\alpha j,c} &= \left.\frac{\partial P_\alpha}{\partial \eta_j}\right|_u = \left.\frac{\partial^2 E}{\partial \mathcal{E}_\alpha \partial \eta_j}\right|_u, \\ e_{\alpha j,i} &= \sum_m \frac{\partial P_\alpha}{\partial u_m}\frac{\partial u_m}{\partial \eta_j}, \\ d_{\alpha j} &= \frac{dP_\alpha}{d\sigma_j} = \sum_i e_{\alpha i}(C^{-1})_{ji}. \end{aligned} \tag{2}$$

Here, σ_i is the stress tensor; η_j is the strain tensor; $e_{\alpha j}$ is the piezoelectric tensor, with subscripts i and c denoting the ionic and clamped ion components, respectively; E is the total energy of the system; $\mathcal{E}_\alpha$ is the imposed electric field vector; u are the atomic displacements from equilibrium; $d_{\alpha j}$ is the piezoelectric strain tensor; and P_α is the polarization vector. Greek indices such as α represent axis directions, and Latin indices such as i, j describe tensor components using Voigt notation.

We apply a symmetry and dimensionality analysis to define in-plane directions and independent components of the elastic and piezoelectric tensors. Plane-wave-based DFT codes such as VASP calculate the C_{ij} and $e_{\alpha j}$ constants based on periodic boundary conditions of a 3D system. Therefore, it is important that these quantities are modified or converted for a 2D case with in-plane stress and strain. For a 2D system, this means that the σ_i and ϵ_j are zero when i or j involves the out-of-plane z direction [8,9]. Also, a renormalization is needed for the elastic and strain tensors such that $C_{ij}^{2D} = a_z C_{ij}^{3D}$ and $e_{ij}^{2D} = a_z e_{ij}^{3D}$, where a_z is the length of the simulation cell in the z-direction. However, the polarization P_α is not restricted to remain in-plane.

We use orthorhombic simulation cells for both lizardite and kaolinite derivatives to calculate elastic and piezoelectric constants as defined in the SI [53]. In these cells, the in-plane lattice parameters along the x-axes were chosen to be longer than the lattice parameters on the y-axes. In all structures, the z-direction is perpendicular to the xy-plane. Lizardites have $3m$ point-group symmetry, hence x and y in-plane directions are identical [8,9]. However, the honeycomb lattice of kaolinites leads to an anisotropy between x and y directions, which was previously noted by Sato *et al.* [65]. Since 2D kaolinite and lizardite crystals have m and $3m$ point group symmetries, respectively, the complete piezoelectric strain tensor can be obtained using only the independent tensor elements. For $3m$ point group symmetry, these are $e_{22} = e_{21} = e_{16}$ and $e_{32} = e_{31}$, and in m point group symmetry these are e_{21}, e_{22}, e_{31}, e_{32}, and e_{16} [66]. In both structures, $e_{11} = e_{12} = 0$.

In Tables VIII and VII, we show that the elastic properties of transition metal silicates are very similar to each other. The main difference is that elastic constants of kaolinites are smaller than the lizardites. This is most likely because the hexagonal vacancy in kaolinites allows additional room for relaxation, leading to smaller elastic moduli. Indeed, a similar conclusion can be made using the bulk forms of kaolinite and lizardite (3D $Al_2Si_2O_9H_3$ and $Mg_3Si_2O_9H_3$, respectively), where C_{11} elastic constants of 200 and 245 GPa were calculated using DFT, respectively [65,67]. Additionally, the C_{11} elastic constants of kaolinites tend to decrease from Cr to Ni kaolinite, whereas in lizardites the trend is the opposite. This can be related to the trends in structural parameters. We find that the average volume of the transition metal octahedra and the in-plane surface area decreases going from Mn to Ni in both structures. This correlates with the reduced atomic size going towards Ni, hence more tightly packed structures and larger elastic constants for the lizardites.

In Tables VIII and VII, piezoelectric and elastic tensor components are reported. The general trends found in these tables are as follows: In both structures, the clamped-ion and relaxed ion piezoelectric constants, e_{ij}, differ dramatically and lead to a change of sign in e_{31} and/or e_{32}. We should mention that the sign of the e_{31} and e_{32} piezoelectric constants depends on the orientation of the 2D layer, i.e., whether the silicate layer is on top of the transition metal oxide layer.

TABLE VII. Elastic coefficients (C_{ij}) and piezoelectric coefficients (e_{ij} and d_{ij}) of 2D kaolinites. By symmetry, $C_{12} = C_{21}$ and $e_{11} = e_{12} = 0$.

	Clamped-ion				*Relaxed-ion*											
	e_{21}	e_{22}	e_{31}	e_{32}	C_{11}	C_{12}	C_{22}	C_{66}	e_{21}	e_{22}	e_{31}	e_{32}	d_{21}	d_{22}	d_{31}	d_{32}
	pC/m				N/m				pC/m				pm/V			
$Cr_2Si_2O_9H_4$	−6.5	−3.5	26.0	38.1	148.9	54.4	132.2	32.8	40.9	68.9	−39.3	−23.9	0.10	0.48	−0.23	−0.08
$Mn_2Si_2O_9H_4$	1.6	−6.7	30.7	41.2	141.1	49.8	125.7	25.8	83.8	82.3	−54.8	−36.9	0.42	0.49	−0.33	−0.16
$Fe_2Si_2O_9H_4$	−7.6	−1.6	24.4	40.3	143.4	52.9	123.9	29.3	41.4	132.0	−40.2	−21.0	0.12	1.11	−0.26	−0.06
$Co_2Si_2O_9H_4$	6.9	−4.7	27.2	38.1	141.5	48.9	117.8	23.8	53.7	53.8	−40.9	−20.2	0.26	0.35	−0.27	−0.06
$Ni_2Si_2O_9H_4$	1.2	8.2	28.4	39.8	138.2	48.3	113.8	29.3	83.1	56.3	−45.2	−24.1	0.50	0.29	−0.29	−0.10

TABLE VIII. Elastic coefficients (C_{ij}) and piezoelectric coefficients (e_{ij} and d_{ij}) of 2D lizardites. By symmetry $C_{12} = C_{21}$, $C_{11} = C_{22}$, $e_{21} = e_{22}$, $e_{31} = e_{32}$, and $e_{11} = e_{12} = 0$.

	Clamped-ion		*Relaxed-ion*						
	e_{22}	e_{32}	C_{12}	C_{22}	C_{66}	e_{22}	e_{32}	d_{22}	d_{32}
	pC/m		N/m			pC/m		pm/V	
$Mn_3Si_2O_9H_4$	0.6	40.2	139.7	54.9	42.0	69.4	−21.5	0.82	−0.11
$Fe_3Si_2O_9H_4$	2.1	42.9	139.0	55.3	41.7	12.8	−35.7	0.15	−0.18
$Co_3Si_2O_9H_4$	3.1	41.5	148.0	62.3	43.8	39.3	−27.2	0.46	−0.13
$Ni_3Si_2O_9H_4$	4.9	36.3	161.8	64.7	48.1	32.2	−35.8	0.33	−0.16

We kept the orientation of layers fixed in all our calculations such that the transition metal oxide layer is always on top. This change of sign was also observed in the e_{33} constants of 3D auxetic piezoelectric crystals and vdW solids [68,69], and it was found that the magnitude of the ionic contribution is typically much larger than the magnitude of the clamped-ion contribution in these auxetic materials. In Ref. [69], it was pointed out that this large ionic contribution is a main character of auxetic piezoelectric materials, and both e_{31} and e_{33} constants are negative. In quasi-2D materials, e_{33} constants can be obtained experimentally [70], but this is challenging for the computational methods. A standard *ab initio* calculation of an isolated quasi-2D layer in vacuum must yield $e_{33} = 0$ since stretching the simulation cell along the z direction is equivalent to adding vacuum to the simulation, which does noât modify the 2D material in any way. To try to extract a value of e_{33} that corresponds approximately to a value that might be obtained by an indentation experiment, we compute e_{33} for the bulk structure (stacked 2D layers along the z-direction). This simplified approach uses the 2D layer as both substrate and indenter, which should give a good order of magnitude estimate and also relative ordering between the e_{33} constants of 2D layers with different cation substitutions. Consult the SI [53] for additional details.

Similar to e_{31} and e_{32} constants, we find that the e_{22} constants in both materials differ significantly between the clamped-ion and relaxed-ion conditions. However, similar observations for the in-plane piezoelectric constants were previously made on a diverse set of 2D materials and found to be related to their mechanical softness and ionic relaxation in the out-of-plane direction [71]. In kaolinites, we find that d_{31} are larger than d_{32} constants in magnitude, which can be correlated to a similar difference in e_{31} and e_{32} constants as a result of the anisotropy observed in these materials. Similarly, d_{32} constants in kaolinites are typically smaller than those of lizardites, however d_{31} constants in each material (in lizardites $d_{31} = d_{32}$) are comparable. The d_{3j} constants in Tables VIII and VII are all smaller than 1 pm/V, which is on par with most quasi-2D materials which all have d_{31} smaller than 1 pm/V, such as Janus-type transition metal dichalcogenides [72], buckled hexagonal III-V compounds [8], and doped graphene [73].

We find that the main contribution to the relaxed ion out-of-plane piezoelectric constants, $e_{3j,i}$, comes from the displacements of the Si and O atoms in the SiO_4 tetrahedra in these structures, which explains the relatively similar performance across different substituents [53]. We analyze the atomic displacements due to strain that contribute to $e_{\alpha j,i}$ using the tensor $A_{mj} = \partial u_m/\partial \eta_j$ in the SI [53]. We find that the SiO_4 tetrahedra move closer to the MO_6 layer with tensile strain, as would be expected from a material with a positive Poisson ratio. Strain in the x ($\equiv 1$) direction induces displacements in the Si-O bond between the SiO_4 tetrahedra and the MO_6 layer such that Si and O atoms in the SiO_4 tetrahedra move up or down collectively. The magnitude of displacements in these atoms is larger compared to the rest of the system.

IV. CONCLUSION

In conclusion, we have presented a detailed theoretical investigation of the thermodynamic, electronic, magnetic, and piezoelectric properties of 2D transition metal silicates, $M_{2-3}Si_2O_9H_n$, where $n = (0, 4)$. We show that these materials can be thermodynamically stable with hydrogenation. The symmetry of these structures dictates that a finite piezoelectric response exists, and we find that it is on par with a wide range of quasi-2D materials that show similar performance. Our long-term goal is to create a material that can possess ferromagnetism (ideally at elevated temperatures) and also has piezoelectric properties, so that the two can be coupled to each other to modulate the magnetic properties. Future studies are needed to compute the coupling of magnetic and piezoelectric properties to the external stimuli such as electric field or strain. Although we find that the magnetic properties of these materials are predominantly antiferromagnetic or weakly ferromagnetic at best, we expect that this materials framework and the facile experimental synthesis methods [18] will allow further engineering of the transition metal layer with a richer chemical phase space and improved possibilities for magnetic ordering.

ACKNOWLEDGMENTS

We acknowledge the Army Research Office Grant No. W911NF-19-1-0371 for the funding of this work and also the computational resources provided by the institutional clusters at Yale University.

[1] K. S. Burch, D. Mandrus, and J.-G. Park, Nature (London) **563**, 47 (2018).

[2] M. Gibertini, M. Koperski, A. F. Morpurgo, and K. S. Novoselov, Nat. Nanotechnol. **14**, 408 (2019).

[3] C. Gong, L. Li, Z. Li, H. Ji, A. Stern, Y. Xia, T. Cao, W. Bao, C. Wang, Y. Wang, Z. Q. Qiu, R. J. Cava, S. G. Louie, J. Xia, and X. Zhang, Nature (London) **546**, 265 (2017).

[4] G. Barcaro and A. Fortunelli, Phys. Chem. Chem. Phys. **21**, 11510 (2019).

[5] H.-C. Cheng, G. Wang, D. Li, Q. He, A. Yin, Y. Liu, H. Wu, M. Ding, Y. Huang, and X. Duan, Nano Lett. **16**, 367 (2016).

[6] K. S. Novoselov, A. Mishchenko, A. Carvalho, and A. H. Castro Neto, Science **353**, 6298 (2016).

[7] A. K. Geim and I. V. Grigorieva, Nature (London) **499**, 419 (2013).

[8] M. N. Blonsky, H. L. Zhuang, A. K. Singh, and R. G. Hennig, ACS Nano **9**, 9885 (2015).

[9] K. A. N. Duerloo, M. T. Ong, and E. J. Reed, J. Phys. Chem. Lett. **3**, 2871 (2012).

[10] B. Huang, G. Clark, E. Navarro-Moratalla, D. R. Klein, R. Cheng, K. L. Seyler, D. Zhong, E. Schmidgall, M. A. McGuire, D. H. Cobden, W. Yao, D. Xiao, P. Jarillo-Herrero, and X. Xu, Nature (London) **546**, 270 (2017).

[11] Y. Zhou, D. Wu, Y. Zhu, Y. Cho, Q. He, X. Yang, K. Herrera, Z. Chu, Y. Han, M. C. Downer, H. Peng, and K. Lai, Nano Lett. **17**, 5508 (2017).

[12] F. Liu, L. You, K. L. Seyler, X. Li, P. Yu, J. Lin, X. Wang, J. Zhou, H. Wang, H. He, S. T. Pantelides, W. Zhou, P. Sharma, X. Xu, P. M. Ajayan, J. Wang, and Z. Liu, Nat. Commun. **7**, 12357 (2016).

[13] A. Belianinov, Q. He, A. Dziaugys, P. Maksymovych, E. Eliseev, A. Borisevich, A. Morozovska, J. Banys, Y. Vysochanskii, and S. V. Kalinin, Nano Lett. **15**, 3808 (2015).

[14] Y. Tian, M. J. Gray, H. Ji, R. J. Cava, and K. S. Burch, 2D Mater. **3**, 025035 (2016).

[15] X. Wang, K. Du, Y. Y. F. Liu, P. Hu, J. Zhang, Q. Zhang, M. H. S. Owen, X. Lu, C. K. Gan, P. Sengupta, C. Kloc, and Q. Xiong, 2D Mater. **3**, 031009 (2016).

[16] N. Cabrera and N. F. Mott, Rep. Prog. Phys. **12**, 163 (1949).

[17] R. Włodarczyk, J. Sauer, X. Yu, J. A. Boscoboinik, B. Yang, S. Shaikhutdinov, and H. J. Freund, J. Am. Chem. Soc. **135**, 19222 (2013).

[18] C. Zhou, X. Liang, G. S. Hutchings, Z. S. Fishman, J.-H. Jhang, M. Li, U. D. Schwarz, S. Ismail-Beigi, and E. I. Altman, Chem. Mater. **31**, 851 (2019).

[19] F. D. Fischer, J. Sauer, X. Yu, J. A. Boscoboinik, S. Shaikhutdinov, and H. J. Freund, J. Phys. Chem. C **119**, 15443 (2015).

[20] E. I. Altman, J. Götzen, N. Samudrala, and U. D. Schwarz, J. Phys. Chem. C **117**, 26144 (2013).

[21] J.-H. Jhang, C. Zhou, O. E. Dagdeviren, G. S. Hutchings, U. D. Schwarz, and E. I. Altman, Phys. Chem. Chem. Phys. **19**, 14001 (2017).

[22] L. Li, H. Tissot, S. Shaikhutdinov, and H. J. Freund, Chem. Mater. **29**, 931 (2017).

[23] L. Lichtenstein, M. Heyde, and H. J. Freund, J. Phys. Chem. C **116**, 20426 (2012).

[24] S. Shaikhutdinov and H. J. Freund, Adv. Mater. **25**, 49 (2013).

[25] H. Tissot, L. Li, S. Shaikhutdinov, and H. J. Freund, Phys. Chem. Chem. Phys. **18**, 25027 (2016).

[26] D. L. Bish, Clays Clay Miner. **41**, 738 (1993).

[27] M. Mellini and P. F. Zanazzi, Am. Mineral. **72**, 943 (1987).

[28] J. M. D. Coey, A. Moukarika, and O. Ballet, J. Appl. Phys. **53**, 8320 (1982).

[29] P. Bayliss, Mineral. Mag. **44**, 153 (1981).

[30] A. Manceau, D. Chateigner, and W. P. Gates, Phys. Chem. Miner. **25**, 347 (1998).

[31] L. G. Dainyak, B. B. Zviagina, V. S. Rusakov, and V. A. Drits, Eur. J. Mineral. **18**, 753 (2006).

[32] P. J. Malden and R. E. Meads, Nature (London) **215**, 844 (1967).

[33] G. L. Woodward, C. L. Peacock, A. Otero-Fariña, O. R. Thompson, A. P. Brown, and I. T. Burke, Geochim. Cosmochim. Acta **238**, 270 (2018).

[34] H. Shirozu and S. W. Bailey, Am. Mineral. **50**, 868 (1965).

[35] G. W. Brindley and H.-M. Wan, Am. Mineral. **60**, 863 (1975).

[36] R. D. White, D. V. Bavykin, and F. C. Walsh, J. Mater. Chem. A **1**, 548 (2013).

[37] O. Ballet and J. M. Coey, J. Phys. Colloq. **39**, C6-765 (1978).

[38] E. I. Parkhomenko, Piezoelectric and pyroelectric effects in minerals, in *Electrication Phenomena in Rocks* (Springer, Boston, 1971), pp. 35–83.

[39] G. Kresse and J. Furthmüller, Comput. Mater. Sci. **6**, 15 (1996).

[40] G. Kresse and J. Furthmüller, Phys. Rev. B **54**, 11169 (1996).

[41] J. P. Perdew, K. Burke, and M. Ernzerhof, Phys. Rev. Lett. **77**, 3865 (1996).

[42] S. L. Dudarev, G. A. Botton, S. Y. Savrasov, C. J. Humphreys, and A. P. Sutton, Phys. Rev. B **57**, 1505 (1998).

[43] A. Jain, G. Hautier, S. P. Ong, C. J. Moore, C. C. Fischer, K. A. Persson, and G. Ceder, Phys. Rev. B **84**, 045115 (2011).

[44] A. Jain, S. P. Ong, G. Hautier, W. Chen, W. D. Richards, S. Dacek, S. Cholia, D. Gunter, D. Skinner, G. Ceder, and K. A. Persson, APL Mater. **1**, 011002 (2013).

[45] J. E. Saal, S. Kirklin, M. Aykol, B. Meredig, and C. Wolverton, J. Mater. **65**, 1501 (2013).

[46] V. Stevanović, S. Lany, X. Zhang, and A. Zunger, Phys. Rev. B **85**, 115104 (2012).

[47] K. A. Persson, B. Waldwick, P. Lazic, and G. Ceder, Phys. Rev. B **85**, 235438 (2012).

[48] L. Wang, T. Maxisch, and G. Ceder, Chem. Mater. **19**, 543 (2007).

[49] O. Kubaschewski, O. Kubaschewski, C. B. Alcock, and P. J. Spencer, *Materials Thermochemistry*, International Series on Materials Science and Technology (Pergamon, New York, 1993).

[50] R. D. King-Smith and D. Vanderbilt, Phys. Rev. B **47**, 1651 (1993).

[51] R. Resta and D. Vanderbilt, Top. Appl. Phys. **105**, 31 (2007).

[52] J. Neugebauer and M. Scheffler, Phys. Rev. B **46**, 16067 (1992).

[53] See Supplemental Material at http://link.aps.org/supplemental/10.1103/PhysRevMaterials.5.104002 for additional information.

[54] A. Narayan, A. Bhutani, S. Rubeck, J. N. Eckstein, D. P. Shoemaker, and L. K. Wagner, Phys. Rev. B **94**, 045105 (2016).

[55] N. Mounet, M. Gibertini, P. Schwaller, D. Campi, A. Merkys, A. Marrazzo, T. Sohier, I. E. Castelli, A. Cepellotti, G. Pizzi, and N. Marzari, Nat. Nanotechnol. **13**, 246 (2018).

[56] *Chemistry of the Elements*, 2nd ed., edited by N. N. Greenwood and A. Earnshaw (Butterworth-Heinemann, Oxford, 1997).

[57] W. A. Dollase, F. Seifert, and H. S. C. O'Neill, Phys. Chem. Miner. **21**, 104 (1994).
[58] K. Persson, Materials Data on Cr_2SiO_4 (SG:70) by Materials Project (2014).
[59] Q. Sun and N. Kioussis, Phys. Rev. B **97**, 094408 (2018).
[60] S. V. Streltsov and D. I. Khomskii, Phys. Rev. B **77**, 064405 (2008).
[61] G. J. Redhammer, G. Roth, W. Treutmann, M. Hoelzel, W. Paulus, G. André, C. Pietzonka, and G. Amthauer, J. Solid State Chem. **182**, 2374 (2009).
[62] M. Berciu and R. N. Bhatt, Phys. Rev. Lett. **87**, 107203 (2001).
[63] H. Shi, H. Pan, Y.-W. Zhang, and B. I. Yakobson, Phys. Rev. B **88**, 205305 (2013).
[64] R. Mishra, W. Zhou, S. J. Pennycook, S. T. Pantelides, and J. C. Idrobo, Phys. Rev. B **88**, 144409 (2013).
[65] H. Sato, K. Ono, C. T. Johnston, and A. Yamagishi, Am. Mineral. **90**, 1824 (2005).
[66] S. V. Gallego, J. Etxebarria, L. Elcoro, E. S. Tasci, and J. M. Perez-Mato, Acta Crystallogr., Sect. A **75**, 438 (2019).
[67] B. Reynard, N. Hilairet, E. Balan, and M. Lazzeri, Geophys. Res. Lett. **34**, L13307 (2007).
[68] S. Liu and R. E. Cohen, Phys. Rev. Lett. **119**, 207601 (2017).
[69] J. Liu, S. Liu, J. Y. Yang, and L. Liu, Phys. Rev. Lett. **125**, 197601 (2020).
[70] C. Cui, F. Xue, W. J. Hu, and L. J. Li, npj 2D Mater. Appl. **2**, 18 (2018).
[71] C. Sevik, D. Çakir, O. Gülseren, and F. M. Peeters, J. Phys. Chem. C **120**, 13948 (2016).
[72] R. Hinchet, U. Khan, C. Falconi, and S. W. Kim, Mater. Today **21**, 611 (2018).
[73] M. T. Ong and E. J. Reed, ACS Nano **6**, 1387 (2012).